Nature Communications

https://doi.org/10.1038/s41467-026-74019-7

Article in Press

Layer-number-parity-dependent abnormal magnetic ordering in few-layer CrI3 on N-face AlN substrate

Received: 22 December 2025

Accepted: 28 May 2026

Cite this article as: Chen, J., Chen, J., Wang, C. *et al.* Layer-number-parity-dependent abnormal magnetic ordering in few-layer CrI3 on N-face AlN substrate. *Nat Commun* (2026). https://doi.org/10.1038/s41467-026-74019-7

Jiamin Chen, Jiahao Chen, Cong Wang, Yi Zhang, Minglai Li, Yanping Li, Jiejun Wu, Tongjun Yu, Wei Ji & Lun Dai

Layer-number-parity-dependent abnormal magnetic ordering in few-layer CrI_3 on N-face AlN substrate

Jiamin Chen[1,2], Jiahao Chen[1], Cong Wang[3], Yi Zhang[1,2], Minglai Li[1,2], Yanping Li[1], Jiejun Wu[1,4], Tongjun Yu[1,4], Wei Ji[3*], Lun Dai[1,2,4*]*

AUTHOR ADDRESS

[1] State Key Lab for Mesoscopic Physics and Frontiers Science Center for Nano-optoelectronics, School of Physics, Peking University, Beijing 100871, China

[2] Collaborative Innovation Center of Quantum Matter, Beijing 100871, China

[3] School of Physics, Key Laboratory of Quantum State Construction and Manipulation (Ministry of Education), Renmin University of China, Beijing 100872, China

[4] Peking University Yangtze Delta Institute of Optoelectronics, Beijing 100871, China

*Correspondence and requests for materials should be addressed to

Lun Dai (email: lundai@pku.edu.cn)

Wei Ji (email: wji@ruc.edu.cn)

Cong Wang (email: wcphys@ruc.edu.cn)

KEYWORDS

abnormal magnetic ordering, reflective magnetic circular dichroism, magnetic multistate switching, magnetic transition critical temperature, N-face AlN substrate

ABSTRACT

The research about two-dimensional van der Waals magnetic materials has advanced the breakthroughs in ultrathin magnetic devices. We experimentally demonstrate that single-crystal N-face AlN polar substrate can program layer-number-parity-dependent magnetic multistates and their evolution sequence in few-layer CrI_3. In odd-layer samples, as 5L-CrI_3/AlN, when $\mu_0 H$ sweeps from 3 to −3 T, the reflective magnetic circular dichroism signal evolves through distinct magnetic multistates (+5 → –1 → +1 → –5), where +1 corresponds to the moment of a spin-up monolayer. Thereby, we vertically program novel magnetic ground states and their evolution sequence via a simplified heterointerface. Our first-principles calculations attribute this effect to interfacial hole doping: it globally reconfigures the magnetic ground state of odd-layer CrI_3 to a novel ferrimagnetic order, and spatially differentiates the interlayer exchange and magnetic anisotropy between the surface/interfacial and interior layers. Our work advances the practical integration and design of two-dimensional magnetic devices with tailored functionalities.

Introduction

The discovery of two-dimensional (2D) van der Waals (vdW) magnetic materials[1,2] has sparked extensive research interest[3-7] and catalyzed breakthroughs in ultrathin magneto-optics and spin-functional devices[8-11]. Since the performances of these devices are fundamentally determined by the specific magnetic configurations[12-15], precisely regulating magnetic configurations is a core prerequisite for advancing the practical application of 2D magnets. Beyond simple ferromagnetic-paramagnetic transitions, layered magnets host a rich spectrum of magnetic polymorphs—distinct magnetic configurations with potentially degenerate energies. The controlled switching between these states represents a new frontier for multi-state memory and magneto-logic devices.

Recent pioneering studies have unveiled key strategies for manipulating such polymorphs. In the layered antiferromagnet CrSBr, a "layer-sharing" effect within lateral homostructures enables deterministic routing of degenerate states, effectively choosing one polymorphic path over another[16]. Complementarily, interfacial charge transfer in vertical heterostructures (e.g., graphene/CrSBr) can lift the degeneracy between polymorphs, allowing their distinct optical identification[17]. These advances mark significant progress in the selection and detection of pre-existing, nearly degenerate magnetic states. However, a more profound level of control—vertically programming novel magnetic ground states and their evolution sequence via a simplified heterointerface—remains an outstanding challenge. Such a capability is crucial for the practical integration and design of 2D magnetic devices with tailored functionalities.

Few-layer CrI_3 exhibits interlayer antiferromagnetism[9,18,19]. The magnetic order of CrI_3 can be strengthened/weakened via electrostatic gating[20,21] and magnetoelectric coupling[22]. The interlayer antiferromagnetic coupling can be transformed into ferromagnetic coupling through static pressure[23].

Moreover, in bilayer CrI_3, the interlayer exchange interaction between antiferromagnetic and ferromagnetic can be tuned by interlayer stacking order[24,25], with the antiferromagnetic coupling arising from a distinct stacking order with C2/m symmetry. Besides, theoretical predictions have proposed several methods to enhance magnetic transition critical temperature T_C for CrI_3[26-34], among which the electronic doping from polar substrates is particularly noteworthy[35,36]. However, to date, none of these methods have been experimentally verified. More importantly, study about the precisely regulating magnetic configurations in few-layer CrI_3 on polar substrates has never been reported.

In this work, we experimentally demonstrate that single-crystal N-face AlN polar substrate can enhance T_C and, more strikingly, program layer-number-parity-dependent magnetic ground states and their evolution sequence in few-layer CrI_3. In odd-layer samples, such as 5L-CrI_3/AlN, when the $\mu_0 H$ sweeps from 3 to −3 T, the reflective magnetic circular dichroism (RMCD) signal evolves through distinct magnetic multistates (+5 → –1 → +1 → –5), where +1 corresponds to the moment of a spin-up monolayer. This abnormal phenomenon is absent in even-layer samples. This programmable magnetic reversal dynamics signifies a step beyond the selection or routing of degenerate polymorphs. First-principles calculations attribute this effect to a dual modulation by interfacial hole doping: it globally reconfigures the magnetic ground state of odd-layer CrI_3 to a novel ferrimagnetic order, and spatially differentiates the interlayer exchange and magnetic anisotropy between surface/interfacial and interior layers. The competition between the modulated magnetic parameters under an external magnetic field leads to the observed layer-selective spin-flip sequence, thereby resulting in the abnormal reversal pathway. Our work demonstrates that, via a simplified heterointerface, both enhancement of T_C and precise modulation of magnetic configurations of CrI_3 can be realized, advancing the practical application of 2D magnets.

Results

Sample fabrication and RMCD measurement

Schematic diagram and optical image of the hBN-encapsulated few-layer-CrI_3/AlN (Sample 1) and the hBN-encapsulated few-layer-CrI_3/SiO_2 (Sample 2) are shown in Fig. 1a–c. Atomic force microscopy shows that the thicknesses of CrI_3 in Samples 1 and 2 are ~4.1 nm (~5 layers) and ~8.1 nm (~10 layers, Supplementary Fig. S1), respectively. Both the magnetic field and excitation light were perpendicular to the sample surface and parallel to the easy magnetization axis of CrI_3. The N-face AlN substrates were cut and polished from a 2-inch wafer-scale AlN single-crystal (see Supplementary Fig. S2a), grown by homemade physical vapor transport (PVT) system[37-39] (see Methods). AlN is a wide-bandgap semiconductor material, which has strong surface polarization[40,41]. Raman spectrum and X-Ray Diffraction (XRD) data of the N-face AlN substrate are shown in Supplementary Fig. S2b–d. The ω-scan rocking curves of the XRD (0002) and $(10\bar{1}2)$ planes exhibit single peaks and narrow full widths at half maximum (FWHMs), indicating the high crystal quality of the AlN substrate.

The RMCD signals (see Methods) versus $\mu_0 H$ relations at various temperatures T for CrI_3/AlN (Sample 1) and CrI_3/SiO_2 (Sample 2) are shown in Fig. 1d and 1e, respectively. These curves exhibit multiple plateaus, corresponding to the spin-flip[42] induced distinct magnetized states under various magnetic fields[10,14]. The plateaus disappear above the T_C. We can see that, for both samples, the coercive field decreases monotonously as the temperature increases. Herein, we define a critical magnetic field ($\mu_0 H_c$), corresponding to the magnetic fields for the maximum spin-flip steps (purple dashed lines in Fig. 1d–e). From the $\mu_0 H_c$ versus T relations in Fig. 1f, we obtain the T_C values to be about 50.0 and 47.5 K for CrI_3 samples on AlN and SiO_2, respectively. Compared to SiO_2 substrate, the AlN substrate causes a 5.3% enhancement to T_C of CrI_3 (see Methods). RMCD signals versus T relations of Samples 1 and 2 at $\mu_0 H$ =

3 T are plotted in Fig. 1g and its inset, respectively. By fitting these scattered data with the function[14,43] $RMCD(T) = RMCD_0(1 - T/T_C)^{\beta}$, we obtain the T_C values to be about 50.2 and 48.1K for CrI_3 samples on AlN and SiO_2, respectively, consistent with the result shown in Fig. 1f. Notably, T_C increases with the number of layers of CrI_3[44]. Therefore, the observation of higher T_C in the thinner CrI_3 on AlN suggests that the T_C enhancement caused by the N-face AlN single-crystal substrate is significant.

N-face AlN substrate induced abnormal layer-number-parity-dependent magnetic ordering evolution

Fig. 2a–b present a magnified magnetic-field-dependent RMCD curve of the 5L-CrI_3/AlN at 15 K, which reveals the abnormal magnetization dynamics. When $\mu_0 H$ sweeps from 3 to −3 T (Fig. 2a), the RMCD signals evolve through distinct magnetic multistates (+5 → –1 → +1 → –5), where +1 corresponds to the moment of a spin-up monolayer. This abnormal magnetic ordering deviates markedly from the expected monotonic stepwise decrease (+5 → +3 → +1 → −1 → −3→ −5) observed in the 5L-CrI_3/SiO_2 sample[45]. Specifically, the magnetic moment exhibits the abnormal behavior at −0.85 T: jumping from −1 (state 2) to +1 (state 3). Similarly, when $\mu_0 H$ sweeps from −3 to 3 T (Fig. 2b), the RMCD signals evolve through distinct magnetic multistates (–5 → +1 → –1 → +5), with the abnormal transition from +1 (state 3) to −1 (state 2) occurring at 0.85 T. This abnormal magnetic state flip phenomenon persists at temperatures below T_C, as shown in Fig. 2c–d. Here, we define the magnetic field for the abnormal state transitions (−1↔+1) as the critical transition magnetic field ($\mu_0 H_{transfer}$), highlighted by the shadowed regions in Fig. 2c and Fig. 2d.

To gain deeper insight into the abnormal magnetic spin-flip phenomenon, we fabricated Sample 3 (Fig. 3a), which contains both odd- and even-layer CrI_3 on AlN substrate, and conducted spatially resolved

RMCD measurements. The thicknesses of the odd- and even-layer CrI_3 are ~5.3 nm (~7 layers) and ~6.1 nm (~8 layers), respectively, as shown in Supplementary Fig. S3. The corresponding RMCD signals versus $\mu_0 H$ curves at 15 K are shown in Fig. 3b. When $\mu_0 H$ sweeps from −3 to 3 T, the abnormal magnetic ordering appears again in the odd-layer CrI_3, but not in the even-layer CrI_3. Specifically, at 1 T, the RMCD signals of the odd-layer and even-layer samples are negative and positive, respectively. At 3 T, the magnetizations for both samples are saturated with stronger positive RMCD signals. To further confirm this phenomenon, we performed RMCD mappings on an area containing both the odd- and even-layer CrI_3 at 1 T (Fig. 3c) and 3 T (Fig. 3d). Again, we can see that, at 1 T, the RMCD signals from the odd- and even-layer CrI_3 regions are negative and positive, respectively. At 3 T, the RMCD signals from both the odd- and even-layer CrI_3 regions are positive.

We further compared the critical transition magnetic fields $\mu_0 H_{transfer}$ for 5L- and 7L-CrI_3 on AlN, as shown in Fig. 3e. For identical temperature, the absolute value of $\mu_0 H_{transfer}$ for 7L-CrI_3 is much smaller than that for 5L-CrI_3, hinting that this abnormal transition may disappear for thicker CrI_3. Besides, the $|\mu_0 H_{transfer}|$ values for both samples decrease as temperature increases. Notably, as temperature increases from 2 to 20 K, $|\mu_0 H_{transfer}|$ decreases by ~36.9%, while $|\mu_0 H_c|$ decreases by only ~8.6% (Fig. 1f), suggesting they have different physical origins.

Physical mechanism of AlN substrate induced magnetic multistate switching

To elucidate the origin of the layer-parity-dependent magnetic multistate switching in few-layer CrI_3, we performed density functional theory (DFT) calculations to investigate the role of the AlN substrate and the layer-number parity. Two heterostructures, composed of a 4-layer (4L) and a 5-layer (5L) CrI_3 with a 4-layer AlN substrate, were used to model the even- and odd-layer cases, respectively. Significant hole transfer from the AlN substrate to the bottom CrI_3 layer is identified at the CrI_3/AlN interfaces in both

heterostructures (-3.6×10^{12} e/cm^2 for 4L and -6.4×10^{12} e/cm^2 for 5L), driven by a large offset between the valence band edges of CrI_3 (−5.9 eV) and AlN (−8.1 eV). The average doping level exhibits a layer-number parity dependence, calculated to be -1.5×10^{-3} e/Cr for 4L and -2.7×10^{-3} e/Cr for 5L systems, indicating a stronger effect in odd-layer CrI_3. As shown in the differential charge density plots and their line profiles (Fig. 4a, b), this hole doping is not uniform. In 5L CrI_3, the interfacial and surface layers exhibit net hole doping, while the three interior layers experience a slight electron doping. This non-uniform distribution arises because the valence band maximum of few-layer CrI_3 is dominated by surface-localized states (Supplementary Fig. S4). The heterostructure also imposes an in-plane biaxial compressive strain of 0.7% on the CrI_3 layers; however, the effect of this strain on the magnetic ground state and anisotropy is minor compared to that of the interfacial charge transfer (see Methods for a quantitative comparison).

This spatially non-uniform charge redistribution simultaneously reconstructs the magnetic ground state. Local hole doping significantly enhances the antiferromagnetic (AFM) coupling between layers[46], particularly for the interface- and surface-proximate layers. Our calculations show that the favored magnetic configuration in 4L (even-layer) CrI_3 retains its free-standing structure, namely A-type AFM one (↓↑↓↑, Supplementary Table S1). The free-standing 5L (odd-layer) CrI_3 is ferrimagnetic through the A-type interlayer AFM coupling. However, introduction of the AlN substrate varies the original ferrimagnetic configuration to another ferrimagnetic configuration with two FM and two AFM interlayer couplings and symmetrically distributed layer magnetization, denoted as FiM-sym (Fig. 4d). The FiM-sym configuration, corresponding to the abnormal ferrimagnetic states observed experimentally, −1 (↑↓↓↓↑) or +1 (↓↑↑↑↓), is 4.1 meV/Cr more favored over the original FiM configuration in energy (Supplementary Table S2). Charge doping calculations on free-standing 5L CrI_3 confirm that a hole doping level matching the interface-induced value indeed switches the magnetic ground state to the FiM-sym configuration (Fig. 4e), validating the interface-doping-driven ground-state transition.

The same non-uniform doping also generates layer-dependent exchange and anisotropy. From the energy differences between magnetic configurations, we quantified the key exchange parameters: the AFM coupling between the surface/interface layers and the interior (J_1 = –1.08 meV/Cr) is significantly stronger than the weak FM coupling within the interior bulk layers (J_2 = 0.40 meV/Cr). Furthermore, the magnetic anisotropy energy (MAE) is highly sensitive to the local doping level[21,47]. As shown in Fig. 4f, the single-ion MAE of monolayer CrI_3 increases sharply with hole doping. The calculated MAE values are 0.14 meV/Cr for the surface layer, 0.25 meV/Cr for the interfacial layer, and 0.11 meV/Cr for the interior layers. For simplicity, we denote the hole-doped surface and interfacial layers collectively by an effective anisotropy D_1 (averaged to 0.20 meV/Cr), and the electron-doped interior layers by D_2 (0.11 meV/Cr).

The magnetic reversal pathway is governed by the interplay of magnetic exchange (J_1 and J_2), anisotropy (D_1 and D_2), and the Zeeman energy (Z). For the two intermediate states observed in our experiment, −1 (↑↓↓↓↑) and +1 (↓↑↑↑↓), the exchange and anisotropy contributions are identical by symmetry, so their relative stability is set by the Zeeman term. However, the actual reversal sequence is governed by kinetics. Fig. 4g illustrates the two competing pathways: the abnormal pathway –5 → +1 → −1 → +5 (blue) observed in our experiment, and the normal pathway –5 → +1 → +5 (red) if thermodynamics alone controlled the process. Starting from the –5 (↓↓↓↓↓) state, the system first flips the three interior layers to arrive at the +1 (↓↑↑↑↓) because the barrier for flipping interior layers ($–2J_1 + 3D_2$) is substantially lower than that for flipping a surface or interfacial layer ($–2J_1 + 2D_1$), a kinetic preference that overrides the thermodynamic favorability of –1 (↑↓↓↓↑). As the field sweeps into the positive regime, the direct +1 → +5 transition faces a high barrier ($2J_1 + 2D_1$) exacerbated by the deep +1 well. In contrast, the abnormal path first visits the metastable –1 (↑↓↓↓↑) state via a cooperative spin-flip with a lower barrier ($2J_1 + 3D_2$), then completes the reversal to +5 (↑↑↑↑↑). Our calculations show that

the abnormal route requires an energy barrier 0.7 meV/Cr lower than the normal route (Fig. 4g, lower panel). A detailed energy decomposition is provided in Supplementary Fig. S5. Through non-uniform charge transfer, it not only changes the global magnetic ground state in odd-layer CrI_3 but also spatially modulates magnetic exchange and anisotropy, thus leading to the layer-selective and parity-dependent switching observed in experiments.

Discussion

We study interfacial modulation of 2D magnetism in hBN-encapsulated few-layer CrI_3 on single-crystal N-face AlN polar substrate by measuring the temperature- and magnetic-field-dependent RMCD signals. We found T_C enhancement of few-layer CrI_3, and more strikingly, the novel magnetic ground states and abnormal magnetic reversal dynamics in odd-layer CrI_3. These phenomena are absent on non-polar substrates. We performed DFT calculations to elucidate the origin of the layer-parity-dependent magnetic multistate switching in few-layer CrI_3 and attribute this effect to a dual modulation by interfacial hole doping. Our work demonstrates a facile substrate engineering for enhancing T_C and manipulating magnetic configurations, advancing the practical application of 2D vdW magnetic materials. Our approach may be applied to other 2D vdW magnets.

Methods

Preparation of the single-crystal N-face AlN substrates.

A homemade physical vapor transport (PVT) system, equipped with a tungsten resistive heater, was employed for AlN single-crystal growth. The growth process was carried out under synergistic control of the thermal and flow fields, in a high-purity nitrogen atmosphere (400–800 mbar pressure range), with a growth temperature ranging from 2150 to 2250 °C. The AlN source was sintered AlN powder which had undergone a high-temperature and low-temperature alternate sintering process, specifically designed to minimize the oxygen impurities. Seed crystals derived from heterogeneous growth processes, exhibiting comparable crystalline quality, were utilized to facilitate homogeneous PVT growth. The AlN source was sublimated at high temperature and transported to the seed crystals under a temperature gradient to form AlN single crystals. The as-grown AlN single crystals were cut into wafers with a diamond wire saw. The wafers underwent surface treatments, including grinding, chemical mechanical polishing at N-face, and acid washing (a phosphoric/sulfuric acid mixture, 180–200 °C), to smooth the surface and remove surface oxides as well as the damaged layer. The AlN crystalline quality was characterized using high-resolution X-ray diffraction (X'PERT-MRD).

Sample fabrication and characterization.

First, CrI_3 and hBN flakes were mechanically exfoliated from their bulk crystals (Shanghai Onway Technology Co., Ltd) on polydimethylsiloxane (PDMS) substrates in an argon gas-filled glove box with < 0.1 ppm concentration of water and oxygen. Then, few-layer CrI_3 and hBN were assembled layer-by-layer on both AlN and SiO_2/Si substrates, with the help of a microscope attached with a micro-manipulator, in the same glove box using the PDMS substrates as stamps. Both the N-face AlN and SiO_2 substrates were pre-coated by Au marks for location purpose. The thicknesses and surface morphologies of the flakes were characterized by an atomic force microscope (Asylum Research, Cypher S). Raman spectra

measurements were performed in a micro-zone confocal Raman system (WITec alpha 300R) under 633 nm laser illumination.

Temperature and magnetic-field-dependent RMCD measurements.

The RMCD measurements were performed in a dry cryostat (attoDRY2100, base temperature of 1.7 K) equipped with a 9 T superconducting magnet and a home tailored microscopic setup. The excitation light (633 nm He-Ne laser), modulated by a chopper (883 Hz) and a photo-elastic modulator (PEM100, 50.051 kHz) to switch between on/off and σ^+/σ^- polarization states, respectively, was focused on the samples with a beam diameter ~2 μm by a low-temperature apochromatic objective (LTAPO/VISIR/0.82). The reflected light from the sample was collected by the same objective into a photomultiplier tube (PMT1001) and processed by a Zurich HF2LI two-channel lock-in amplifier. The RMCD signal was determined as $\frac{\text{PEM modulated AC signal}}{\text{Chopper modulated AC signal}}$. The RMCD mappings were conducted by using a modular piezo motion controller (ANC300) to move the sample stage. The critical magnetic fields were extracted from the partial differential (d(*RMCD*)/d($\mu_0 H$)) peak values of the *RMCD*–$\mu_0 H$ curves. The error bars are obtained from the full-width at half-maximum (FWHM) of these peaks[21]. The net magnetizations of few-layer CrI_3 are determined by the RMCD signal. For example, given the RMCD signal magnitude representing the magnetic moment of +5 (−5) for 5-layer CrI_3 under saturated magnetization of 3 T (−3 T), the magnetic moments associated with other RMCD plateaus can accordingly be determined based on the plateau heights and positions.

DFT calculations.

The calculations were performed using the generalized gradient approximation and projector augmented-wave method as implemented in the Vienna ab initio calculation package[48]. Dispersion correction was considered in Grimme's semiempirical D3 scheme[49] in combination with the PBE functional (PBE-D3).

This combination achieves an accuracy comparable to that of the optB86b-vdW functional for describing the geometric properties of layered materials at a lower computational cost[50]. On-site Coulomb interactions on Cr 3*d* orbitals are characterized via U and J values, namely, $U = 3.9$ eV and $J = 1.1$ eV, as revealed via a linear response method[51-53] via the PlusU package. A uniform Monkhorst–Pack *k*-mesh of size 15×15×3 was adopted for integrating over the Brillouin zone of a CrI_3 bulk unit cell. The shape and volume of the unit cell of pristine CrI_3 were fully optimized, and all the atoms were allowed to relax until the residual force per atom was less than 0.01 eV/Å. A 4×4 CrI_3/9×9 AlN (0001) magnetic supercell was adopted for the calculations of structure optimization and magnetic ground state (Fig. 4) to include the substrate effect, in which an MP *k*-mesh of 1×1×1 was used. This heterostructure results in an optimal in-plane biaxial compressive strain of 0.7% to CrI_3. A kinetic energy cutoff of 400 eV for the plane-wave basis set was used for both structural relaxation and electronic structure calculations of the heterostructure models. A sufficiently large vacuum layer over 20 Å along the out-of-plane direction was adopted to eliminate the interaction among layers. The bottom surface of the AlN slab was passivated with pseudo-hydrogen atoms carrying a fractional charge of 1.25e to saturate the dangling bonds of the Al atoms and eliminate spurious electric fields arising from the polar surface.

Calculation of interfacial charge transfer.

The interfacial charge transfer density was obtained from DFT calculations through the following procedure. First, we calculated the differential charge density by subtracting the charge densities of the isolated CrI_3 slab and the isolated AlN slab from those of the fully relaxed CrI_3/AlN heterostructure. Second, we performed an in-plane integration of this differential charge density over the xy plane to obtain the line profile of charge redistribution as a function of the out-of-plane coordinate z, as shown in Fig. 4a–b. Third, to quantify the net charge transferred to the entire CrI_3 slab or to individual CrI_3 layers, we performed a volume integration of the differential charge density over the corresponding spatial regions.

The spatial extent of each CrI_3 layer was defined by the z-positions of the I atoms at its top and bottom boundaries.

Analysis of interfacial strain effect.

To disentangle the effects of strain and charge transfer, we performed additional calculations on a free-standing 5L CrI_3 model with the atomic coordinates preserved from the relaxed CrI_3/AlN heterostructure, thereby retaining the 0.7% in-plane compressive strain but excluding charge transfer. In this strained free-standing model, the A-type AFM configuration remains slightly lower in energy than the FiM-sym configuration by only 0.01 meV/Cr—a negligible difference within DFT accuracy. In contrast, the full CrI_3/AlN heterostructure favors the FiM-sym configuration by 0.73 meV/Cr, confirming that charge transfer, not strain, drives the ground-state transition. We also calculated the single-ion magnetic anisotropy energy (MAE) of monolayer CrI_3 under 0.7% compressive strain. The MAE increases marginally from 0.115 meV/Cr (unstrained) to 0.119 meV/Cr, a change of less than 3%, whereas hole doping at levels comparable to the interface more than doubles the MAE (Fig. 4f). Thus, the modulation of magnetic parameters in our system is dominated by interfacial charge transfer.

DATA AVAILABILITY

Source Data that support the findings of this study are provided with this paper.

ASSOCIATED CONTENT

Supplementary Information Available:

Fig. S1. Optical and Atomic force microscopy characterizations of Samples 1 and 2.

Fig. S2. Optical image, Raman spectrum, and X-Ray Diffraction curves of a typical single-crystal N-face AlN substrate.

Fig. S3. Atomic force microscope characterizations of Sample 3.

Fig. S4. Layer decomposed electronic band structure of free-standing 5L-CrI_3.

Fig. S5. Energy contribution of competing magnetic reversal pathways in 5L-CrI_3 on AlN.

Table S1. Relative total energies of the substrate-supported 4L-CrI_3.

Table S2. Relative total energies of the substrate-supported 5L-CrI_3.

REFERENCES

1. Gong, C. *et al.* Discovery of intrinsic ferromagnetism in two-dimensional van der Waals crystals. *Nature* **546**, 265-269 (2017).
2. Huang, B. *et al.* Layer-dependent ferromagnetism in a van der Waals crystal down to the monolayer limit. *Nature* **546**, 270-273 (2017).
3. Tan, C. *et al.* Hard magnetic properties in nanoflake van der Waals Fe3GeTe2. *Nat. Commun.* **9**, 1554 (2018).
4. Otrokov, M. M. *et al.* Prediction and observation of an antiferromagnetic topological insulator. *Nature* **576**, 416-422 (2019).
5. Lee, K. *et al.* Magnetic Order and Symmetry in the 2D Semiconductor CrSBr. *Nano Lett.* **21**, 3511-3517 (2021).
6. Ferrenti, A. M. *et al.* Change in Magnetic Properties upon Chemical Exfoliation of FeOCl. *Inorg. Chem.* **59**, 1176-1182 (2020).
7. Grzeszczyk, M. *et al.* Strongly Correlated Exciton-Magnetization System for Optical Spin Pumping in CrBr3 and CrI3. *Adv. Mater.* **35**, 2209513 (2023).
8. Wang, Z. *et al.* Very large tunneling magnetoresistance in layered magnetic semiconductor CrI3. *Nat. Commun.* **9**, 2516 (2018).
9. Song, T. C. *et al.* Giant tunneling magnetoresistance in spin-filter van der Waals heterostructures. *Science* **360**, 1214-1218 (2018).
10. Klein, D. R. *et al.* Probing magnetism in 2D van der Waals crystalline insulators via electron tunneling. *Science* **360**, 1218-1222 (2018).
11. Yan, Z., Zhang, R. Q., Dong, X. L., Qi, S. F. & Xu, X. H. Significant tunneling magnetoresistance and excellent spin filtering effect in CrI3-based van der Waals magnetic tunnel junctions. *Phys. Chem. Chem. Phys.* **22**, 14773-14780 (2020).
12. Song, T. C. *et al.* Spin photovoltaic effect in magnetic van der Waals heterostructures. *Sci. Adv.* **7**, 36 (2021).
13. Chen, J. *et al.* Spin-Enhanced Self-Powered Light Helicity Detecting Based on Vertical WSe2–CrI3 p–n Heterojunction. *ACS Nano* **18**, 26261-26270 (2024).
14. Cheng, X. *et al.* Light helicity detector based on 2D magnetic semiconductor CrI3. *Nat. Commun.* **12**, 6874 (2021).
15. Chen, J. M. *et al.* Optical Helicity and Polarization Dependent NIR Negative Photocurrent in the 2D Magnetic Semiconductor CrI3. *Adv. Opt. Mater.* **12**, 2301488 (2024).
16. Sun, Z. Y. *et al.* Resolving and routing magnetic polymorphs in a 2D layered antiferromagnet. *Nat. Mater.* **24**, 226-233 (2025).
17. Hong, C. Y. *et al.* Charge transfer governed interlayer magnetic coupling and symmetry breaking in a van der Waals magnet. *Nat. Commun.* **16**, 9498 (2025).
18. Kim, H. H. *et al.* Evolution of interlayer and intralayer magnetism in three atomically thin chromium trihalides. *P Natl. Acad. Sci. USA* **116**, 11131-11136 (2019).
19. Sun, Z. *et al.* Giant nonreciprocal second-harmonic generation from antiferromagnetic bilayer CrI3. *Nature* **572**, 497-501 (2019).
20. Huang, B. *et al.* Electrical control of 2D magnetism in bilayer CrI3. *Nat. Nanotechnol.* **13**, 544-548 (2018).
21. Jiang, S., Li, L., Wang, Z., Mak, K. F. & Shan, J. Controlling magnetism in 2D CrI3 by electrostatic doping. *Nat. Nanotechnol.* **13**, 549-553 (2018).

22. Jiang, S., Shan, J. & Mak, K. F. Electric-field switching of two-dimensional van der Waals magnets. *Nat. Mater.* **17**, 406-410 (2018).
23. Song, T. *et al.* Switching 2D magnetic states via pressure tuning of layer stacking. *Nat. Mater.* **18**, 1298-1302 (2019).
24. Sivadas, N., Okamoto, S., Xu, X. D., Fennie, C. J. & Xiao, D. Stacking-Dependent Magnetism in Bilayer CrI3. *Nano Lett.* **18**, 7658-7664 (2018).
25. Jiang, P. H. *et al.* Stacking tunable interlayer magnetism in bilayer CrI3. *Phys. Rev. B* **99** (2019).
26. Peng, X. B., Su, M. S. & Gao, D. Q. Controllable high Curie temperature through 5d transition metal atom doping in CrI3. *Chinese. Phys. B* **33**, 017503 (2024).
27. Chen, G. X. *et al.* Electronic structure and magnetic properties of CrI3 monolayer doped by rare earth metal atoms. *J Phys. Chem. Solids* **187**, 111838 (2024).
28. Ai, W., Hu, X. H., Yang, J., Lu, C. H. & Sun, L. T. Selective sensing properties and enhanced ferromagnetism in CrI3 monolayer via gas adsorption. *Nanotechnology* **34**, 065202 (2023).
29. Wu, S. J., Li, A. L., Wang, Y. P. & Ouyang, F. P. Half-metallicity and Curie temperature enhancement of CrI3 through boron atoms adsorption. *Superlattice. Microst.* **159**, 107054 (2021).
30. Webster, L. & Yan, J. A. Strain-tunable magnetic anisotropy in monolayer CrCl3, CrBr3, and CrI3. *Phys. Rev. B* **98**, 144411 (2018).
31. Xu, J. L. *et al.* Strain enhanced magnetism of V-implanted CrI3 monolayer. *Appl. Phys. Lett.* **122**, 063101 (2023).
32. Liao, J. J. *et al.* Spin reorientation and Curie temperature promotion in CrI3-Bi van der Waals heterostructures. *Phys. Rev. B* **107**, 184403 (2023).
33. Chen, S. B. *et al.* Boosting the Curie Temperature of Two-Dimensional Semiconducting Crl3 Monolayer through van der Waals Heterostructures. *J Phys. Chem. C* **123**, 17987-17993 (2019).
34. Hu, A. M., Zhang, X. H., Luo, H. J. & Xiao, W. Z. Half-metallicity and enhanced Curie temperature of Ti-embedded CrI3 monolayer. *Mater Today Commun* **25**, 101438 (2020).
35. Liu, N. S., Zhou, S. & Zhao, J. J. High-Curie-temperature ferromagnetism in bilayer CrI3 on bulk semiconducting substrates. *Phys. Rev. Mater.* **4** (2020).
36. Zhu, H. Y., Gao, Y. F., Hou, Y. S., Gui, Z. G. & Huang, L. Tunable magnetic anisotropy in two-dimensional CrX3/AlN (X = I, Br, Cl) heterostructures. *Phys. Rev. B* **106**, 134412 (2022).
37. Chen, J. H. *et al.* Synergistic Effect of Thermal and Flow Fields on Stress Distribution in AlN Crystal Growth by PVT. *Cryst. Growth. Des.* **25**, 2691-2699 (2025).
38. Chen, J. H. *et al.* Surface Control of AlN Single Crystal Growth on SiC Substrate. *Cryst. Growth. Des.* **24**, 4801-4809 (2024).
39. Chen, J. H. *et al.* Optimization of AlN Crystal during Iterative PVT Growth. *Cryst. Growth. Des.* **26**, 1866-1874 (2026).
40. Sumathi, R. R. Review-Status and Challenges in Hetero-epitaxial Growth Approach for Large Diameter AlN Single Crystalline Substrates. *Ecs. J Solid State Sc.* **10**, 035001 (2021).
41. Bernardini, F., Fiorentini, V. & Vanderbilt, D. Spontaneous polarization and piezoelectric constants of III-V nitrides. *Phys. Rev. B* **56**, 10024-10027 (1997).
42. Paudel, T. R. & Tsymbal, E. Y. Spin Filtering in CrI3 Tunnel Junctions. *ACS Appl. Mater. Interfaces* **11**, 15781-15787 (2019).
43. Fei, Z. Y. *et al.* Two-dimensional itinerant ferromagnetism in atomically thin Fe3GeTe2. *Nat. Mater.* **17**, 778-782 (2018).
44. Huang, B. *et al.* Emergent phenomena and proximity effects in two-dimensional magnets and heterostructures. *Nat. Mater.* **19**, 1276-1289 (2020).

45. Liu, Z. *et al.* Observation of intrinsic crystal phase in bare few-layer CrI3. *Nanophotonics-Berlin* **11**, 4409-4417 (2022).
46. Jiang, P. H. *et al.* Stacking tunable interlayer magnetism in bilayer CrI3. *Phys. Rev. B* **99**, 144401 (2019).
47. Kim, J. *et al.* Exploitable Magnetic Anisotropy of the Two-Dimensional Magnet CrI3. *Nano Lett.* **20**, 929-935 (2020).
48. Kresse, G. & Furthmüller, J. Efficient iterative schemes for ab initio total-energy calculations using a plane-wave basis set. *Phys. Rev. B* **54**, 11169 (1996).
49. Grimme, S., Antony, J., Ehrlich, S. & Krieg, H. A consistent and accurate ab initio parametrization of density functional dispersion correction (DFT-D) for the 94 elements H-Pu. *J. Chem. Phys.* **132**, 154104 (2010).
50. Liu, N. *et al.* Competing multiferroic phases in monolayer and few-layer NiI_2. *Phys. Rev. B* **109**, 195422 (2024).
51. Wang, Y. *et al.* Strain-Sensitive Magnetization Reversal of a van der Waals Magnet. *Adv. Mater.* **32**, 7 (2020).
52. Cococcioni, M. & De Gironcoli, S. Linear response approach to the calculation of the effective interaction parameters in the LDA+U method. *Phys. Rev. B* **71**, 035105 (2005).
53. Wu, Y. *et al.* Fe-Intercalation Dominated Ferromagnetism of van der Waals Fe_3GeTe_2. *Adv. Mater.* **35**, 2302568 (2023).

ACKNOWLEDGMENTS

We acknowledge the National Key Research and Development Program of China (No. 2022YFA1604302 and No. 2023YFA1406500) and the National Natural Science Foundation of China (Nos. 62174005, 62234003, 92477205 and 5246116032) for supporting this work. Calculations were performed at the Physics Lab of High-Performance Computing (PLHPC) and the Public Computing Cloud (PCC) of Renmin University of China.

FUNDING

L.D. discloses support for the research of this work from the National Key Research and Development Program of China (No. 2022YFA1604302) and the National Natural Science Foundation of China (No. 62174005). W.J. and C.W. disclose support for the research of this work from the National Key Research and Development Program of China (No. 2023YFA1406500) and the National Natural Science

Foundation of China (Nos. 92477205 and 5246116032). T.J.Y. discloses support for the research of this work from the National Natural Science Foundation of China (No. 62234003).

AUTHOR INFORMATION

Corresponding Author

Lun Dai − State Key Lab for Mesoscopic Physics and Frontiers Science Center for Nano-optoelectronics, School of Physics, Peking University, Beijing 100871, China; Email: lundai@pku.edu.cn

Wei Ji − School of Physics, Key Laboratory of Quantum State Construction and Manipulation (Ministry of Education), Renmin University of China, Beijing 100872, China; Email: wji@ruc.edu.cn

Cong Wang − School of Physics, Key Laboratory of Quantum State Construction and Manipulation (Ministry of Education), Renmin University of China, Beijing 100872, China; Email: wcphys@ruc.edu.cn

Author Contributions

L.D. and J.M.C. conceived the project. J.M.C. fabricated the samples and conducted the measurements. J.M.C. and L.D. performed data analysis. C.W and W.J. performed the DFT theoretical calculations. J.H.C. prepared the single-crystal N-face AlN substrates and performed XRD measurements. Y.Z., M.L.L. and Y.P.L. prepared the metal electrodes and conducted the AFM measurements. J.J.W and T.J.Y helped with the growth of AlN single-crystal in PVT system. L.D. supervised this research. J.M.C., L.D., C.W., and W.J. wrote the manuscript. All authors contributed to discussion.

Competing interests

The Authors declare no competing interests.

Figure Legends

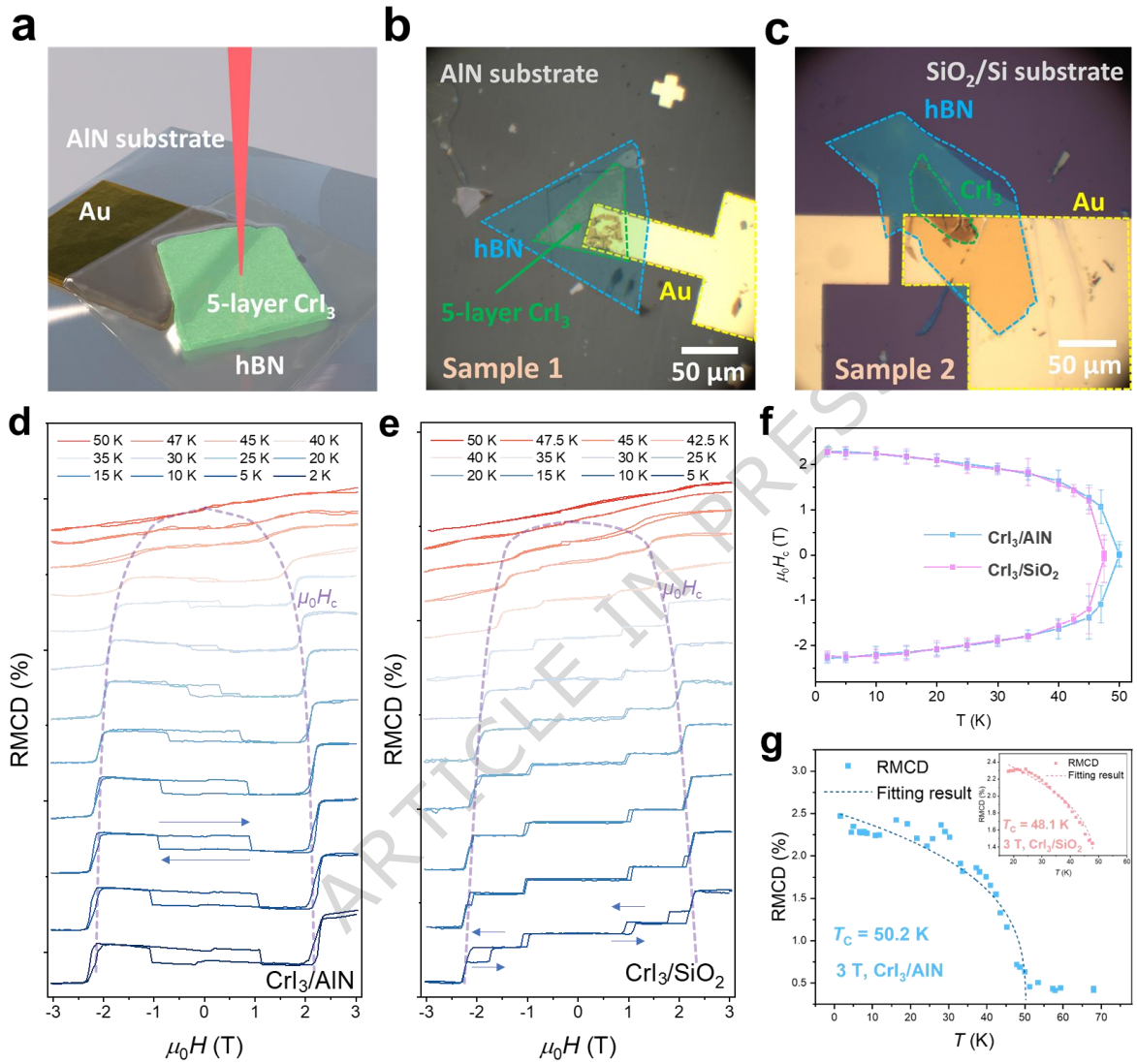

Fig. 1 | Morphologies and RMCD measurements of the samples. Schematic diagram (**a**) and optical image (**b**) of the hBN encapsulated 5L-CrI_3/AlN (Sample 1). **c**, Optical image of the 10L-CrI_3/SiO_2 (Sample 2). The hBN layers were used to protect the samples from degradation. The green, blue, and yellow dashed lines in **b** and **c** demarcate the CrI_3, hBN, and Au mark, respectively. Temperature-dependent RMCD signals of Sample 1 (**d**) and Sample 2 (**e**). These curves exhibit multiple plateaus,

corresponding to the spin-flip induced distinct magnetized states under various magnetic fields. The spin-flip steps disappear above T_C. We define a critical magnetic field ($\mu_0 H_c$), which corresponds to the magnetic fields for the maximum spin-flip steps denoted by the purple dashed lines. **f**, The critical magnetic fields $\mu_0 H_c$ versus T relations for Sample 1 (blue line) and Sample 2 (pink line). The obtained T_C values are about 50.0 and 47.5 K for CrI_3 samples on AlN and SiO_2, respectively. From these curves, we can obtain that the T_C increases by ~5.3% when using AlN versus SiO_2 substrate. **g**, The RMCD signal versus T relation for the CrI_3/AlN at $\mu_0 H$ = 3 T (scattered data). Inset: The *RMCD–T* relation of the CrI_3/SiO_2 at $\mu_0 H$ = 3 T. By curve fitting these data with the function $RMCD(T) = RMCD_0(1 - T/T_C)^{\beta}$ (dashed line), we obtain the T_C values to be about 50.2 and 48.1K for CrI_3 samples on AlN and SiO_2, respectively, consistent with the experimental result depicted in (**f**).

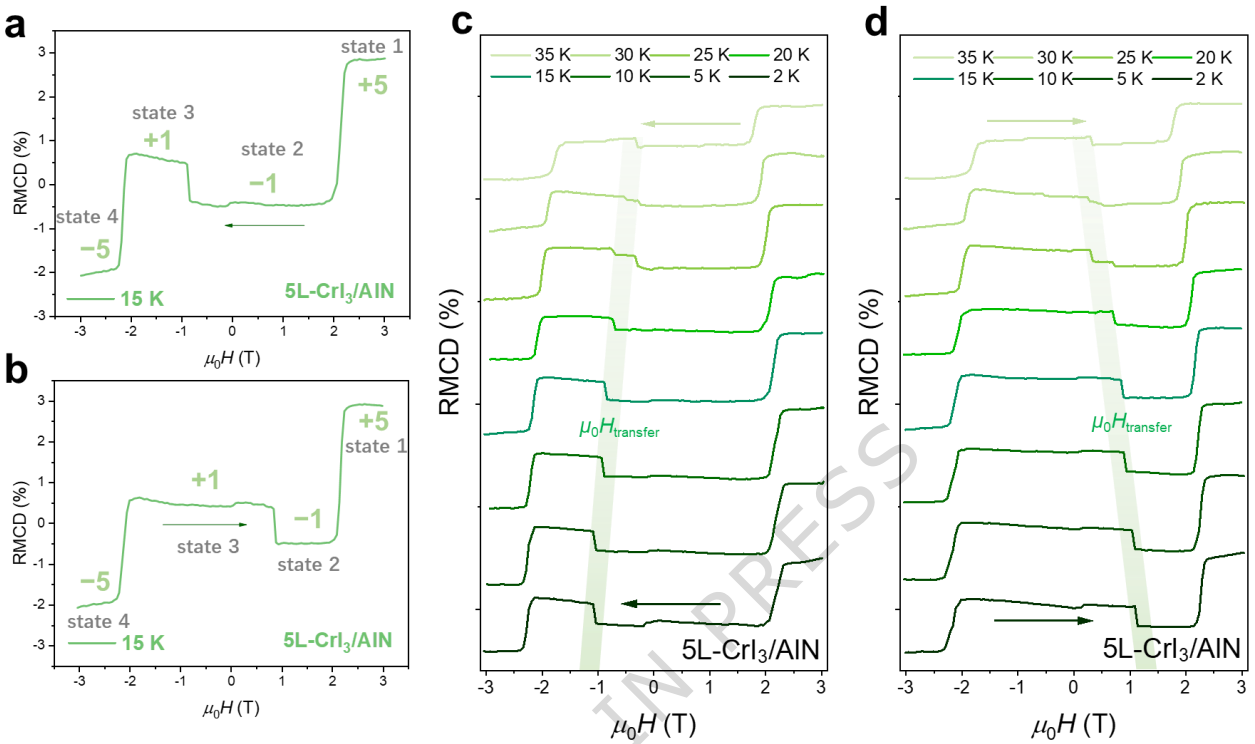

Fig. 2 | N-face AlN substrate-induced abnormal magnetic ordering. The RMCD signals versus $\mu_0 H$ curves of the 5L-CrI_3/AlN during magnetic field descending (**a**) and ascending (**b**), measured at 15 K. When $\mu_0 H$ sweeps from 3 T to −3 T, the RMCD signals evolve through distinct magnetic multistates (+5 → –1 → +1 → –5), where +1 corresponds to the moment of a spin-up monolayer. Specifically, the magnetic moment exhibits an abnormal behavior at −0.85 T: jumping from −1 (state 2) to +1 (state 3). Similarly, when $\mu_0 H$ sweeps from −3 to 3 T, the RMCD signals evolve through distinct magnetic multistates (–5 → +1 → –1 → +5), with the abnormal transition from +1 (state 3) to −1 (state 2) occurring at 0.85 T. This abnormal magnetic ordering deviates markedly from the expected stepwise monotonic variation observed in the CrI_3/SiO_2 sample. The RMCD signals versus $\mu_0 H$ curves of the 5L-CrI_3/AlN during magnetic field descending (**c**) and ascending (**d**) under various temperatures. Herein, we define a critical transition magnetic field ($\mu_0 H_{transfer}$), which corresponds to the magnetic fields for the abnormal

state transitions (−1↔+1, i.e., transitioning from states 2 to 3 in **a** and from states 3 to 2 in **b**), highlighted by the shadowed regions.

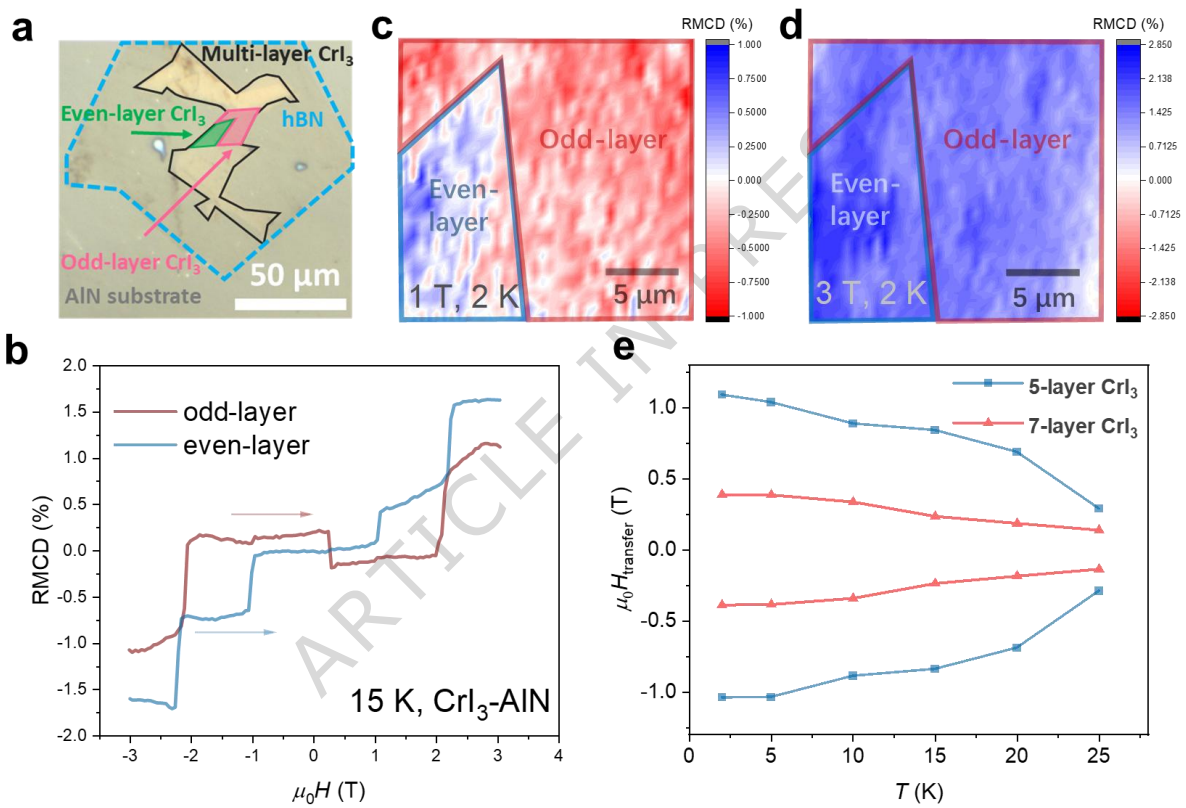

Fig. 3. | The relation between the abnormal magnetic ordering and the parity of number of layers. **a**, Optical image of Sample 3, fabricated by exfoliating a CrI_3 flake which contains both odd- (pink area) and even-layer CrI_3 (green area) on the identical N-face AlN. The odd- and even-layer CrI_3 are ~7 and ~8 layers, respectively. Black and blue lines demarcate multi-layer CrI_3 and hBN, respectively. **b**, The RMCD signal versus $\mu_0 H$ curves for the odd- and even-layer CrI_3 measured at 15 K. When $\mu_0 H$ sweeps from −3 to 3 T, the abnormal magnetic ordering appears again in the 7L-CrI_3, while not in the 8L-CrI_3.

Specifically, at 1 T, the magnetizations of 7L- and 8L-CrI_3 samples are negative (RMCD signal < 0) and positive (RMCD signal > 0), respectively. At 3 T, the magnetizations for both samples are saturated with stronger positive RMCD signals. RMCD mappings on an area containing both odd- and even-layer CrI_3 at 1 T (**c**) and 3 T (**d**). At 1 T, the RMCD signals from the entire 7L-CrI_3 region are negative (red region) and those from the 8L-CrI_3 region are positive (blue region). At 3 T, the RMCD signals from both the 7L- and 8L-CrI_3 regions are positive, and the average magnetization value of the 7L-CrI_3 is lower than that of the 8L-CrI_3. **e**, Temperature-dependent $\mu_0 H_{transfer}$ values for 5L- and 7L-CrI_3 on the N-face AlN. As temperature increases, all the $|\mu_0 H_{transfer}|$ values reduce and approach zero. For identical temperature, the absolute value of $\mu_0 H_{transfer}$ for 7L-CrI_3 is much smaller than that for 5L-CrI_3, indicating that this abnormal transition might disappear for thicker CrI_3. As the temperature increases from 2 to 20 K, $|\mu_0 H_{transfer}|$ decreases by ~36.9%, while $|\mu_0 H_c|$ decreases by only ~8.6% (Fig. 1f), suggesting they have different physical origins.

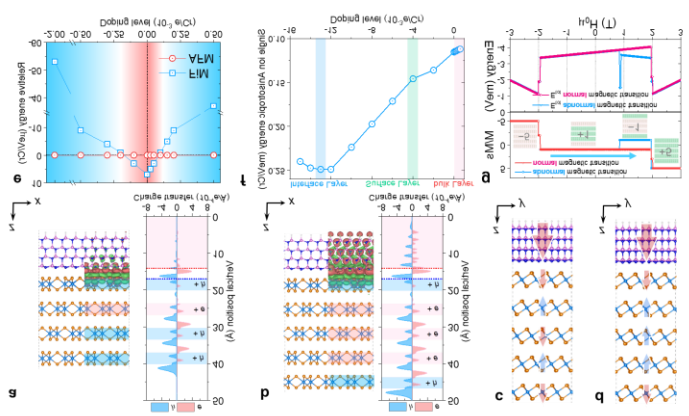

Fig. 4. | Substrate modulated magnetism of few-layer CrI_3. Hetero-interlayer differential charge density and corresponding line profiles along z of the CrI_3 tetralayer (**a**) and pentalayer (**b**) stacked on the AlN substrate. An isosurface value of 0.0005 e $Bohr^{-3}$ was used. The red isosurface contours represent charge accumulation after layer stacking. The blue, green, orange, pink, blue and white balls represent the Cr atoms, I atoms, Al atoms, N atoms and pseudohydrogen atoms, respectively. **c**–**d**, Schematic representations of interlayer magnetic orders, including A-type AFM (**c**) and FiM (**d**) are depicted. The blue and red arrows represent two antiparallel orientations of magnetic moments. **e**, Relative total energies of the FiM (blue rectangles) and AFM (red circles) orders of 5L CrI_3 with different doping levels. The reference zero is chosen as the energies of the AFM order. **f**, Single-ion magnetic anisotropy energy (MAE) of monolayer CrI_3 as a function of doping level. The doping levels corresponding to different layers in the 5L CrI_3/AlN heterostructure are indicated by different colors. **g**, Net magnetic moment, total energy and corresponding magnetic configurations along the abnormal pathway (blue, –5 → +1 → –1 → +5) and the normal pathway (red, –5 → +1→ +5) during a magnetic field sweep from –3 T to +3 T.

Editor's Summary
The authors demonstrate that N-face AlN substrate induces layer-number-parity-dependent magnetic multistates in CrI3. 5L-CrI3/AlN evolves through distinct magnetic multistates , first-principles calculations attribute this effect to interfacial hole doping.

Peer review information: *Nature Communications* thanks the anonymous reviewer(s) for their contribution to the peer review of this work. A peer review file is available.